Mechanical Properties and Multiscale Characterization of Nanofiber–Alumina/Epoxy Nanocomposites

G. M. Brown, F. Ellyin

Department of Materials Engineering, University of British Columbia, #309-6350 Stores Road, Vancouver V6T 1Z4, British Columbia, Canada

Received 3 August 2009; accepted 19 April 2010
DOI 10.1002/app.32662
Published online 18 August 2010 in Wiley Online Library (wileyonlinelibrary.com).

ABSTRACT: In contrast to the bulk of published nanocomposite studies, in this study we investigated the mechanical properties of alumina/epoxy nanocomposites manufactured with nanofillers having a fiber or whisker morphology. The article describes how ultrasonic dispersion and *in situ* polymerization were used to incorporate these 2–4 nm diameter fibers (with aspect ratios of 25–50) into a two-part epoxy resin (Epon 826/Epicure 9551). The use of untreated and surface-modified nanoparticles is contrasted, and improvements in both the tensile strength and modulus were observed at low filler loadings. Microstructural characterization of the nanocomposites via multiscale digital image analysis was used to interpret the mechanical properties and was found to be useful for direct comparison with other nanocomposites. In addition, superior performance was demonstrated through comparisons with numerous nanocomposites with nanoparticle reinforcements ranging from carbon nanofibers to spherical alumina particles. © 2010 Wiley Periodicals, Inc. J Appl Polym Sci 119: 1459–1468, 2011

Key words: mechanical properties; microstructure; nanocomposites; particle size distribution; structure–property relations

INTRODUCTION

The superior properties of polymeric nanocomposites result from the high specific surface areas of their nanoscale reinforcements. This permits significant polymer–filler interaction and a substantial interphase region and, combined with the theoretical homogeneity possible at this scale, offers mechanical properties markedly different from that of the neat polymer. Moreover, these effects can be achieved at low particle loadings, typically on the order of a few volume percentage.

A broad range of nanoparticles are now available, yet only a few materials/morphologies have been extensively used in nanocomposites. Of these, the bulk of polymer reinforcement has been done by layered silicates (clays),[1] which must be separated into individual 1 nm thick plates to take advantage of specific particle surface areas of up to 750 m^2/g.[2] Carbon nanotubes,[3] with typical lengths of 0.5–100 μm, have been similarly used for their exceptional strength and stiffness. Spherical particles are also commonly used and are generally metal oxides of silica,[4–9] alumina,[10–16] zirconia,[17,18] and titanium dioxide.[19,20] These can have all three dimensions in the nanoscale, although their low aspect ratio lowers their reinforcing efficiency through reduced shear loading and fewer opportunities for polymer chain restriction/entanglement.

In contrast, recent reviews of nanocomposites[21,22] have highlighted the dearth of new materials formed with nanoparticles with a whisker or fiber morphology. Of these, the most common have been carbon nanofibers (CNFs)[23–27] and microcrystalline cellulose.[28,29] In one of the few reports of ceramic nanofiber-based nanocomposites,[30,31,32] Yang et al.[32] contrasted the reinforcing effect of alumina nanofibers in polycarbonate and polystyrene with nanospheres, finding considerable increases in both the tensile strength and stiffness. In another article, Miyagawa et al.[30] described the reinforcement of a biobased epoxy by 5 wt % alumina–nanowhiskers. The resulting nanocomposites had an increased storage modulus over that of the neat epoxy, a reduced toughness, and fracture surfaces revealing the agglomeration of particles.

In fact, dispersion homogeneity has been identified as a key aspect of successful nanocomposite preparation,[21] and numerous authors[7,10,11,13,16,19,26,30,33–37] have reported the presence of various degrees of filler heterogeneity that either limited the benefits of nanoscale fillers by reducing the effective nanodispersed phase or constituted potential strength-limiting defects. The sol–gel synthesis of spherical silica nanoparticles in epoxy,[4–6] most notably by Hanse Chemie AG (Geesthacht, Germany), has opened the door for future nanocomposites with both higher filler contents and high levels of particle dispersion. However, their

Correspondence to: F. Ellyin (fernand@composites.ubc.ca).
Contract grant sponsor: National Science and Engineering Research Council of Canada.

application to most polymer systems is limited, and the use of high-aspect-ratio reinforcement is currently outside the scope of this approach. Consequently, the need to understand the impact of heterogeneity remains of great importance when the structure–property relationships in such nanocomposites are assessed.

A key tool in the characterization of both particle size distribution and microstructure is the digital analysis of images obtained via scanning electron microscopy (SEM) and transmission electron microscopy (TEM).[1] This approach originated in studies of microscale reinforcement[38–40] and was found to be similarly effective at elucidating the nanoscale morphology of clays required for modeling these nanocomposites.[2,41] However, the hierarchical nature of nanocomposites also entails the need to capture structural information over a range of length scales. This has been pointed out in several articles,[35,40,42] and methodologies for conducting such multiscale analyses were effectively described by Sheng et al.[43] Recent studies[42,44–46] have built on these works and extended the use of digital image analysis to the nonclay reinforcement of nanocomposites.[9,47]

In this study, we report the mechanical properties of alumina/epoxy nanocomposites formed with commercially available nanofibers and a two-part epoxy resin system. Expanding on previous results,[31] we used a digital-image-based analysis technique to quantitatively characterize the nanoparticle dispersions, with particular attention placed on evaluating the heterogeneity. Comparisons were made between reinforcements using as-received and surface-modified alumina. The differences between the properties resulting from fiber and spherical morphologies are discussed, and the fracture surfaces are described to explain the improvements in both the tensile modulus and strength. In addition, mechanical properties changes were investigated in the context of the particle distributions.

EXPERIMENTAL

Materials

Alumina powder was supplied by Argonide Corp. (Sanford, CA) in the form of 80 nm average diameter spheres and 2–4 nm diameter $\times$ 50−100 nm long fibers. Characterization by Fourier transform infrared spectroscopy (Nicolet-Magna IR spectrometer 750; GMI Inc., Minneapolis, Minnesota) and X-ray photoelectron spectroscopy (AXIS 165 Spectrometer with an α-K source; Kratos Analytical Ltd., Manchester, UK) evidenced high levels of surface hydration with a significant portion of the material being an amorphous boehmite form. Both powders were slightly agglomerated in the as-received state, with the fibers having a bulk density of about 710 kg/m^3 with an unagglomerated specific surface area of 700 m^2/g. Surface modification was achieved with a 3-2-aminoethylaminopropyl trimethoxysilane (APS) supplied by Sigma-Aldrich (Oakville, Canada). The epoxy was a two-part liquid monomer system, consisting of an Epon 826 DGEBA epoxy resin and an Epicure 9551 non-methylenedianiline (non-MDA) polyamine hardener (Resolution Performance Products, Houston, TX).

Nanocomposite preparation

Surface modification of the alumina nanoparticles was conducted in deionized water at pH 4; the pH value was lowered with 0.1% acetic acid. Silane was added in an amount calculated to provide monolayer coverage for the mass of powder treated, with a concentration of slightly less than 0.5 wt %. The as-received nanoparticles were initially dehydrated at 200°C for 2 h. Upon cooling under a nitrogen blanket, they were magnetically stirred into the acidified water/silane mixture, with 20 kHz of ultrasonic energy used for dispersion (Branson 450 Sonifer in pulsed mode; Branson Ultrasonics Corp., Danbury, CT). Mixing was continued until a stable dispersion was achieved, and the treated particles were removed from suspension by a centrifuge (Beckman J2 at 20 kx; Beckman Coulter Inc., Brea, CA). The particles were rinsed twice in methanol and/or acetone and then dried and postcured at 110°C for 1 h before they were stored under nitrogen. Confirmation of the surface modification was made by a comparison of the microscopic Fourier transform infrared spectra of the pristine and treated powders.

Neat epoxy control specimens were prepared for the preheated amine hardener and epoxy resin, combined in a ratio of 100 : 36 by weight. The preheating permitted rapid mixing of the two components, a lower initial viscosity (for enhanced removal of air bubbles and other volatiles), and improved regulation of the gel time. The mixed resin was poured into a preheated, mold-released steel mold, and the epoxy castings were cured at 70°C for 70 min, followed by a postcure at 120°C for 2.5 h.

Nanocomposite specimens were prepared for the pristine (untreated) spherical and fiber forms of the alumina and for both forms of the surface-modified particles. The pristine alumina particles were initially dehydrated for several hours at 110°C before they were cooled to room temperature. Addition to the preheated hardener was made by a magnetic stirrer. Dispersion was achieved with the addition of ultrasonic energy, with an ice bath to maintain a constant temperature. For some series, a settling stratification process and additional vacuum

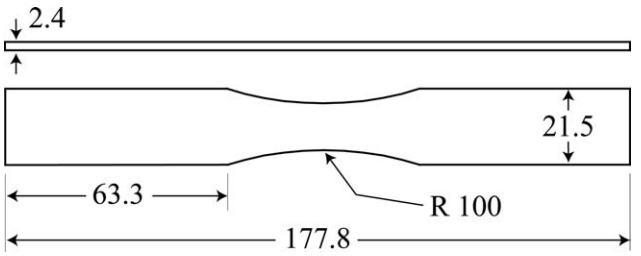

Figure 1 Geometry of the full-sized, tensile test specimens; all dimensions are in millimeters.

degassing steps were added to aid the dispersion process. The nanoparticle-filled hardener was combined with the epoxy in a ratio of 100 : 36 by unfilled weight. The two components were subsequently blended with a high-shear impeller (Nordstone Inc., Wyncote, PA) and additional ultrasonic energy. Casting and curing were conducted as for the neat resin samples.

Relatively large nanocomposite specimens were computer numerical control (CNC)-machined from the middle third of the cast plates with a vacuum table to hold the specimens and achieve the desired tolerances. The constant-radius gauge length, full-sized dog-bone specimen was suitable for loading where failure within a limited region was desired.[48] Its geometry is detailed in Figure 1. Specimens made from cast nanocomposite plates containing spherical particles were designated as S series, and those casts from fibers were designated as F series. Nanocomposites of the APS-surface-modified particles were prefixed with an A. These series are summarized in Table I.

Mechanical testing

Monotonic tensile testing was conducted under load control with a 45 N/s load ramp, with resulting strain rates on the order of 10^{-4} s^{-1}. Tests were performed at room temperature (neat epoxy glass-transition temperature $\approx$ 110°C) in a 45-kN MTS 810 frame with hydraulic wedge grips (MTS, Eden Prairie, MN) and a Teststar IIs DAQ system (MTS). The strain was determined by an extensometer (MTS). Five to ten tensile specimens were tested per data series. Additional fracture testing was conducted to permit the elucidation of the fracture mechanisms. We precracked the fracture specimens by lowering a razor blade a defined distance into the specimen, perpendicular to the loading direction. The crack length and a sharp crack condition were optically determined before failure and correlated by examination of the fracture surfaces via SEM (JEOL 6301F field emission scanning electron microscope; JEOL, Tokyo, Japan). High-magnification evaluations of alumina distribution and homogeneity were made with TEM micrographs (Philips/FEI Morgagni TEM, Hillsboro, Oregon) of sections microtomed perpendicular to the specimen length.

Digital image analysis

Digital images for particle size distribution and morphology characterization were taken at magnifications of 1.8 to 70,000× with a minimum image size of 2000 × 1600 pixels. At each magnification, multiple images were randomly selected across the sample area to capture regional variations in morphology. Preprocessing in Adobe Photoshop was used for conversion to a 16-bit unsigned grayscale and to level the image contrast for accurate thresholding. Segmentation and analysis of the particle attributes, termed *blob analysis,* was completed with Matrox Inspector v4.1 software (Matrox Imaging, Dorval, Canada). Pixel/length-scale conversions of the measurements were made with correlations with image scale bars and known magnifications.

With the measured area of each particle, a corresponding effective circular diameter (ECD) was derived.[40] The analysis created a histogram of particle-specific densities (particle count per unit area on the basis of image areas) with logarithmically spaced bins across the distribution of ECDs for each image. At each magnification, the accurate detection of small particles was limited by the effective resolution of the image[49] and sensitive to artifacts from the thresholding procedure. Similarly, accurate counting of large particles was constrained by the size of the image, the use of an exclusion zone at the image boundaries,[50] and the requirement of large numbers of samples to reduce the statistical error. To preserve accuracy, a confidence interval of particle diameters was established for each analysis scale; this resulted in particle distributions truncated at the ECD extremes.

Subsequent multiresolution compilations were created by integration of the truncated distributions into a full-scale distribution for the nanocomposite under consideration.[35,40,42] Specific subdistributions

TABLE I
Summary of the Manufactured Alumina/Epoxy Nanocomposites, Including Neat Epoxy Resin (E) as a Reference

Series	Nanoparticle	Surface treatment	Filler loading	
			wt %	vol %
E	None	None	0	0
F1	Fiber	None	4.20	1.42
F2	Fiber	None	6.18	2.12
S1	Spherical	None	8.40	2.92
AF1	Fiber	APS	2.16	0.72
AF2	Fiber	APS	2.88	0.96
AF3	Fiber	APS	4.35	1.48

(specific particle densities) were averaged between images of common magnification and scaled with the smallest particle counts as references. Under the assumption of random distributions of particles, area fractions were used synonymously as volume fractions (V_f's).[40,41] Consequently, distributions were adjusted to bulk values,[38] which incorporated the effects of known thresholding errors and corrections for agglomerated particle interior densities less than unity. The full-scale particle size distributions, therefore, incorporated all particles sizes from 3 nm to 100 μm.

RESULTS AND DISCUSSION

Particle distributions and microstructural characterization

TEM images of the nanocomposites revealed an extensive finely dispersed phase with slight agglomeration in all series, as illustrated in Figure 2. Area-normalized frequency (specific frequency) histograms obtained from the digital image analyses quantified the particle size distributions and supported the visual findings.

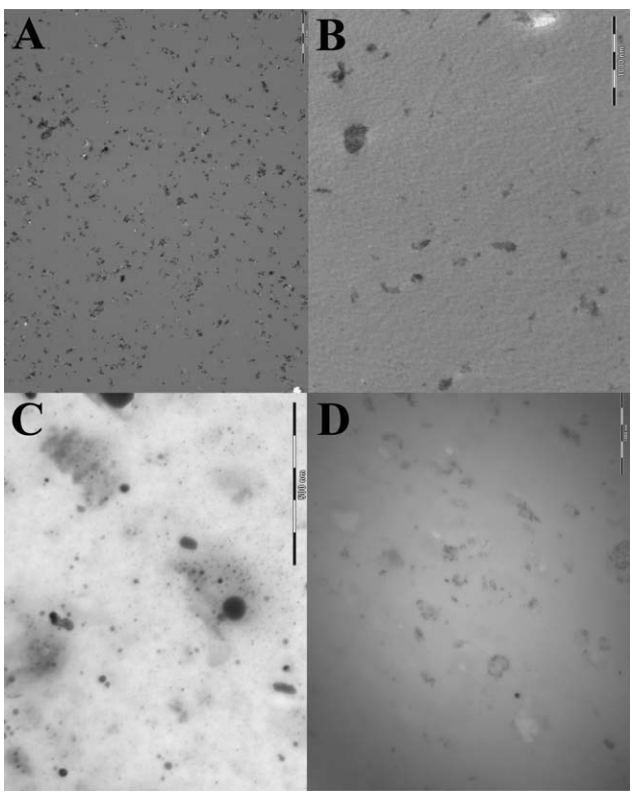

Figure 2 Visual assessment of alumina nanoparticle distribution with TEM images: (A) S1, (B) F1, (C) AF1, and (D) AF3. For images A and C, the scale bar is 500 nm; for images B and D, the scale bar is 1 μm.

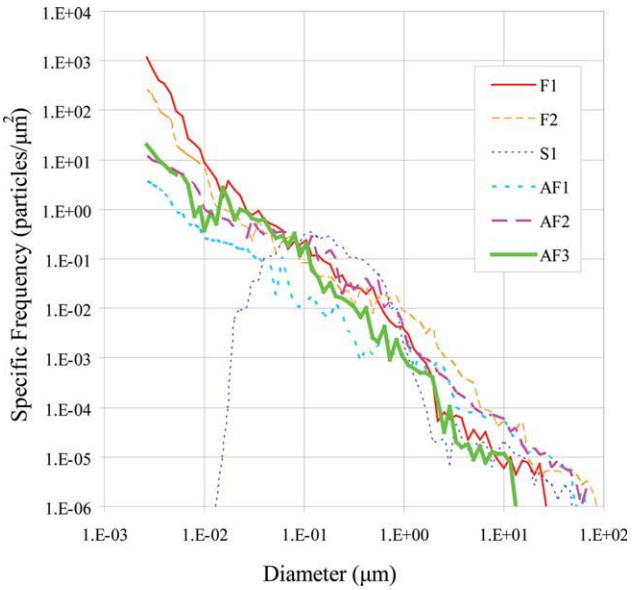

Figure 3 Histogram of alumina nanoparticle distributions: log–log representation of the specific particle density versus diameter for particle sizes from about 3 nm to 100 μm. [Color figure can be viewed in the online issue, which is available at wileyonlinelibrary.com.]

A log–log specific frequency histogram of the particle ECDs is shown in Figure 3; this figure shows large numbers of fibers well dispersed, particularly in the F1 and F2 series of untreated alumina. The distribution for spherical particles peaked at about 100 nm; this corresponded closely to the manufacturer's report primary particle size, which indicated a large number of monodispersed particles or very small agglomerates [cf. Fig. 2(A)]. The graph also points to infrequent agglomerates of larger size, ranging from 10 μm in the AF3 series to 150 μm in the F2 series. Regions of the distributions with sparse or unavailable data were estimated with distribution trendlines.

A more intuitive representation of the distributions is provided in Figure 4, where the V_f of each segment of the distribution is plotted against the associated particle diameter. This graph was obtained by calculation of the area fraction of particles in any given bin across the histogram, with the logarithmic-average diameter. Distributions were corrected to bulk V_f values, which could be obtained from Figure 4 through summation of the V_f contributions for each particle size.

Figure 4 shows that the F1, S1, and AF3 series had the majority of their particles dispersed at the nanoscale, with S1 having an isolated grouping of large agglomerates. The distribution also revealed that the F1 series had the most well-dispersed particle fraction, whereas the F2 series fibers were agglomerated around the micrometer level and higher. Surface-

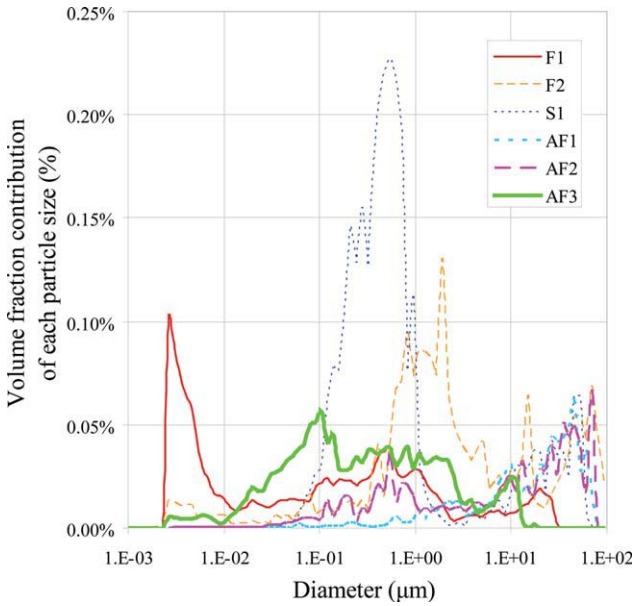

Figure 4 V_f distributions for alumina in the Al_2O_3/epoxy nanocomposites, revealing the contribution of each particle size to the overall V_f. [Color figure can be viewed in the online issue, which is available at wileyonlinelibrary.com.]

modified alumina fiber nanocomposites showed an increasing fraction of fibers dispersed at the nanoscale as V_f increased (AF1→AF3), with the AF3 series exhibiting the fewest and smallest agglomerates (75% of V_f nanodispersed). Although the frequency of agglomerates was up to nine orders of magnitude lower than that of the finely dispersed particle fraction, this minor heterogeneity significantly detracted from V_f of the finely dispersed phase (cf. the 10–100-μm regions of Figs. 3 and 4). The implications of this are discussed more fully in the following section.

Mechanical properties

Representative stress–strain curves for the nanocomposites are shown in Figure 5, with that for neat epoxy included for comparison. The mechanical properties, normalized with respect to those of neat epoxy, are summarized in Table II. The results are based on series averages, with a minimum of three samples failing at the specimen waist. The reliability of the data was indicated by the coefficient of variation (COV) of each test series in conjunction with the p values from student t tests with 95% confidence intervals.

For the untreated particles [S1, F1, and F2; Fig. 5(A)], an improvement in the elastic modulus was observed over neat epoxy, although as the nanoparticle loading increased, this improvement decreased. The strength was reduced for all untreated nanoparticle series compared with that of the neat epoxy. In contrast, for those series with surface-modified particles [AF1, AF2, and AF3; Fig. 5(B)], improvements in both the tensile strength and modulus were demonstrated. These improvements were also shown to increase with increasing V_f of alumina.

Mechanisms of reinforcement

The micrographs of the fracture surfaces aided the interpretation of the mechanical property changes discussed previously by providing mechanisms for nanoparticle reinforcement of the epoxy matrix.

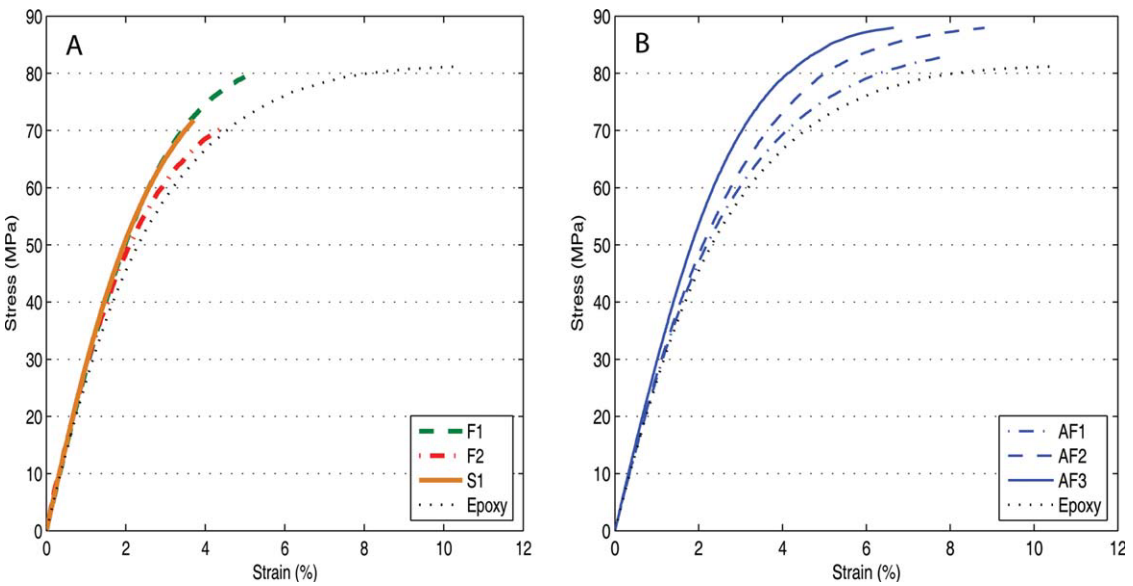

Figure 5 Tensile stress–strain response of the alumina/epoxy nanocomposites. For the sake of clarity, the results were divided into two parts: (A) untreated nanoparticle series S1, F1, and F2 and (B) surface-modified nanoparticle series AF1, AF2, and AF3. [Color figure can be viewed in the online issue, which is available at wileyonlinelibrary.com.]

TABLE II
Mechanical Properties of Alumina/Epoxy Nanocomposites Containing Nanofiber or Nanospherical Particles Normalized with Respect to Neat Epoxy

		Elastic modulus			Failure strength		
Series	Alumina (vol %)	E/E_{Epoxy}	COV (%)	p	σ/σ_{Epoxy}	COV (%)	p
E	0.00	1.00	3.3	–	1.00	4.5	–
F1	1.42	1.19	5.6	<0.001	0.98	3.6	0.649
F2	2.12	1.15	0.2	<0.001	0.89	1.8	0.013
S1	2.92	1.13	1.8	<0.001	0.88	4.1	0.013
AF1	0.72	1.05	1.8	0.024	1.04	1.7	0.182
AF2	0.96	1.09	0.2	0.002	1.11	1.5	0.010
AF3	1.48	1.17	0.2	<0.001	1.12	1.5	0.009

COVs were calculated for each series; the p values were from unpaired student t tests with epoxy using 95% confidence intervals.

E, tensile elastic modulus of the respective series; E/E_{Epoxy}, tensile elastic modulus of the neat epoxy series; σ, tensile strength of the respective series; and σ/σ_{Epoxy}, tensile strength of the neat epoxy series.

Reference should be made to Figure 4 for the corresponding particle distributions.

In this study, the alumina without APS surface modification embrittled the epoxy, restricting mechanisms of plastic deformation without providing the strengthening of load transfer to and sharing by the particles. The nanocomposites, thus had decreased strength compared with the neat epoxy. As shown in Figure 6, the fracture surfaces of the S1 series showed increased roughness over the neat epoxy (A) as a result of the distributed

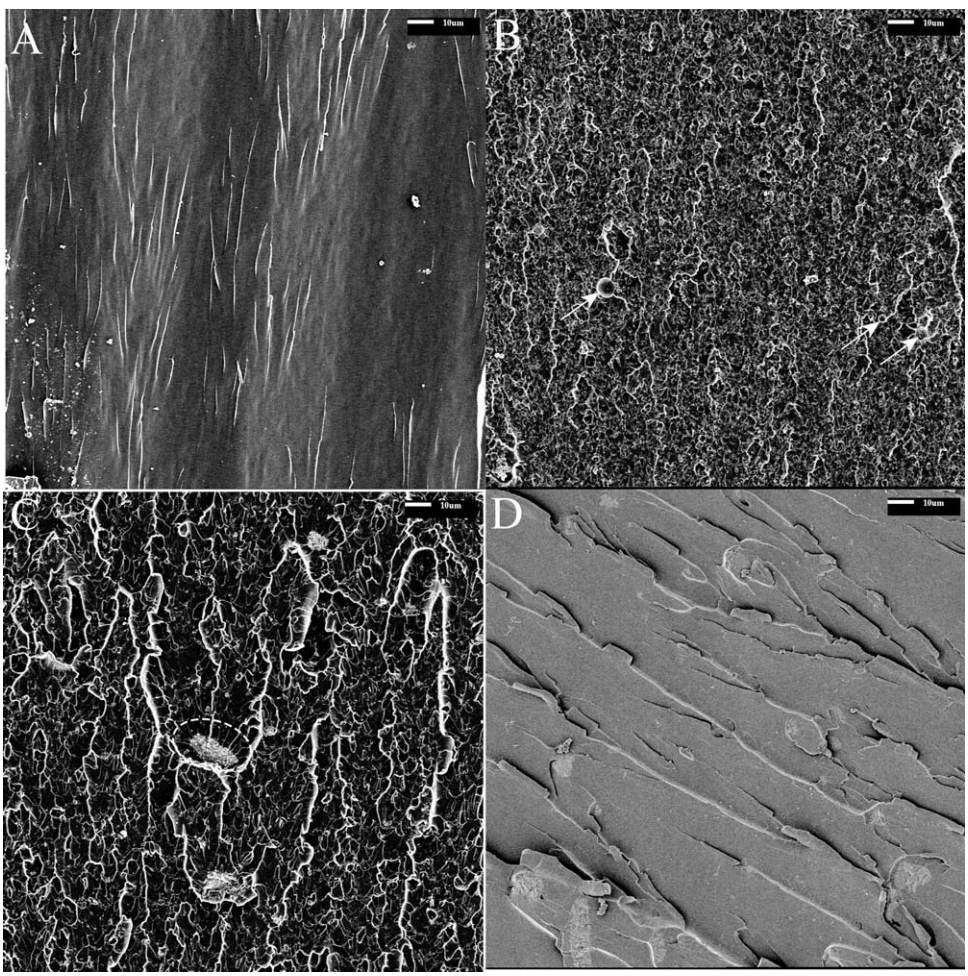

Figure 6 Roughness of the nanocomposite fracture surfaces compared with (A) neat epoxy; (B) S1, showing debonding (white arrows); (C) F1, showing secondary crack front propagation (ellipse); and (D) AF3. The scale bars are 10 μm.

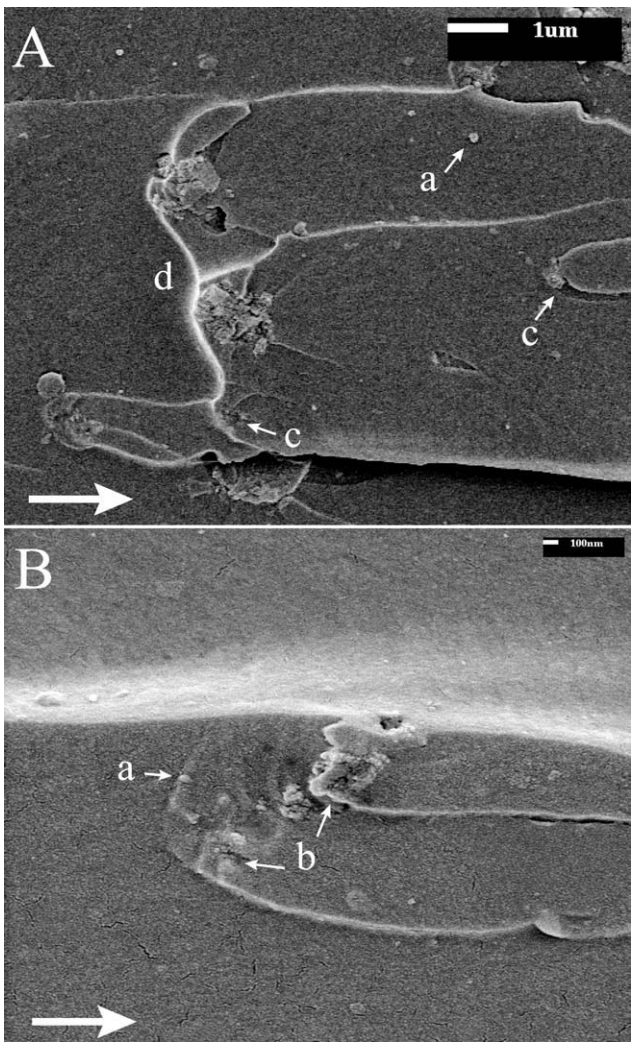

Figure 7 Fracture surfaces of the AF3 series nanocomposites, showing reinforcement at the nanoscale: (A) scale bar = 1 μm with crack pinning by cohesive (d) 1-μm and (c) 300-nm agglomerates and (B) scale bar = 100 nm with (a) crack-tip interaction with 20-nm particles and (b) crack deflection by 200-nm agglomerates. Large arrows indicate the direction of crack propagation.

spherical particles (B) yet lacked indications of extensive offplane fracture mechanisms. Although some evidence was found for void formation in the vicinity of the particles, which was put forward as a toughening mechanism,[6] there were frequent indications of particle debonding (S1 series, B, white arrows) and secondary crack fronts emanating from regions of poor particle wetting or weak agglomerates (F1 series, C, demarcated with an ellipse). Despite this and perhaps because of the compressive state of stress from cure-induced shrinkage, a significant elastic modulus improvement was still evident.

Fracture surfaces of the surface-modified alumina reflected the smaller fraction of well-dispersed fibers with a lower corresponding surface roughness [cf. AF3 series in Fig. 6(D) vs 6(C)]. Higher magnification views taken of the AF3 series nanocomposites are provided in Figure 7 as representative of the treated fiber series. These reveal enhanced particle wet-out (a), crack deflection at the nanoscale (b), and cohesive agglomerates, which promoted deflection of the crack to other planes (c) and crack-tip pinning (d). These indicated enhanced particle–polymer interactions with increased load transfer to the alumina and concomitant strengthening of the epoxy. Also, a reduction in the presence of larger agglomerates, particularly with the AF3 series, decreased the likelihood of defect-containing agglomerates promoting crack initiation and propagation. (For in-depth discussions of the contribution of individual mechanisms to property modification, see Johnsen et al.,[6] Zhao et al.,[11] and others[4,23]).

Comparisons of particle distribution

The influence of particle distributions was explored, although a comparison of the mechanical properties described in this study to the results of other studies is available in the literature. As few articles have described the properties of nanofiber alumina reinforced composites, this comparison also provides context for the improvement using this morphology. Figure 8 depicts the modulus versus V_f values for other spherical and fiber nanoparticle based

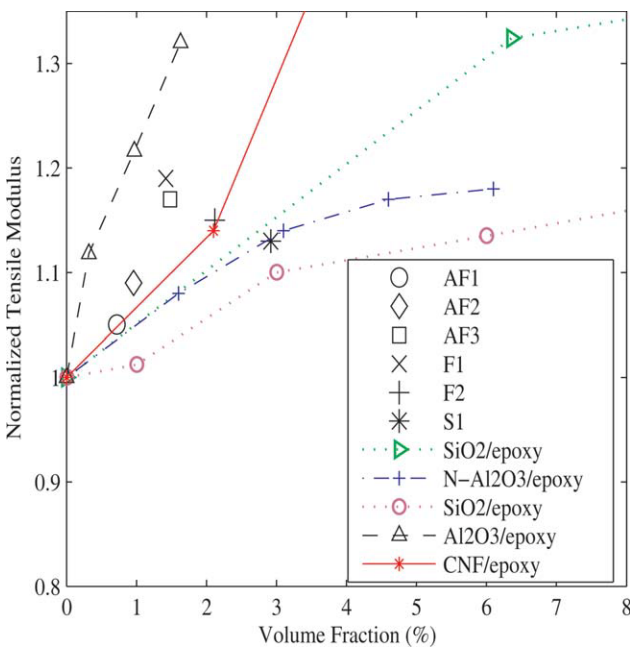

Figure 8 Modulus versus V_f of alumina for these results compared with the reported trends for various fiber and particle nanocomposites. Sources: Ma[8] (dotted arrow), Zhao[11] (dashed dotted +), Zhang[5] (dotted circle), Chen[15] (dashed triangle), and Iwahori[25] (solid asterisk). The N prefix represents untreated particles. [Color figure can be viewed in the online issue, which is available at wileyonlinelibrary.com.]

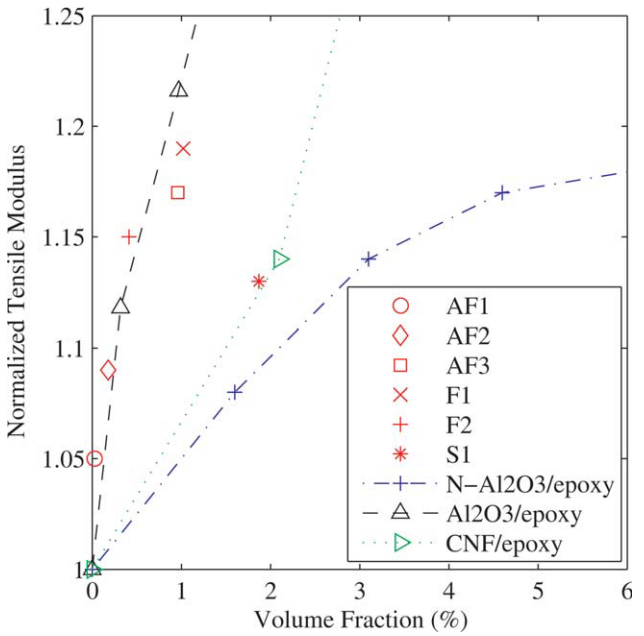

Figure 9 Modulus versus adjusted V_f for these data, reflecting a theoretical particle distribution consisting of only nanoscale particles with ECD $\leq$ 500 nm. The results are contrasted with those for 20–30-nm treated spherical alumina (dashed),[15] 45-nm untreated spherical alumina (dashed dotted +),[11] and CNF (dotted).[25] [Color figure can be viewed in the online issue, which is available at wileyonlinelibrary.com.]

nanocomposites, with the current data overlaid. As previously described, the unmodified series showed an increased modulus, which decreased with increasing V_f, whereas that for the surface-modified nanofiber series showed an increasing modulus with increasing V_f.

The dotted lines in Figure 8 show data for monodispersed spherical SiO_2/epoxy nanocomposites, which showed stiffness improvements comparable to that for series S1 (asterisk), although they were lower than those of the series with nanofiber alumina, F1 and F2. The gains from the superior dispersion of SiO_2 particles in these studies was offset by the lower stiffness of the silica compared with alumina. The dashed dotted curves represent reinforcement with as-received spherical alumina (nonsurface modified; prefixed with an N). The data for the S1 series, also of unmodified spherical alumina, fell directly on this curve; this suggested a similarity in reinforcing efficiency, although Zhao et al.'s[11] nanoparticles were slightly smaller (45 nm diameter).

The curve for CNF reinforcement fell through the middle of the data for nanocomposites of nanofiber alumina. As shown in Figure 5, the three closest series (AF1, AF2, and F2) had only a moderate fraction of fibers at the nanoscale, with agglomerates at length scales similar to the dimensions of the CNFs themselves. In contrast, the F1 and AF3 series, with the best distributions of nanofibers, had higher moduli, with improvements of 19 and 17%, respectively. The proximity of the untreated and surface-modified series also showed that surface modification of the alumina was not necessary for improvements in modulus. However, the data fell below that of Chen et al.'s[15] alumina nanocomposites (dashed triangles), consisting of small spherical particles 10–30 nm in diameter. These were, nonetheless, larger than the nanofiber alumina and should provide correspondingly less reinforcement when at the same degree of dispersion, for the previous discussion implied that enhanced dispersion leads to greater stiffening (via more frequent filler–polymer interactions and greater polymer chain restriction).

To gain insight into the effect of the distribution on the mechanical properties, the known distributions of the nanofiber alumina series were truncated to correspond with that reported in Chen et al.'s study, where a heterogeneity on the order of 500 nm (maximum agglomerate diameter) was present. This was done under the assumption that larger agglomerates had less influence on the modulus than the more finely dispersed fibers. Hence, the impact of these large agglomerates was regarded as negligible, and only particles 500 nm or less in size were counted. The associated modulus

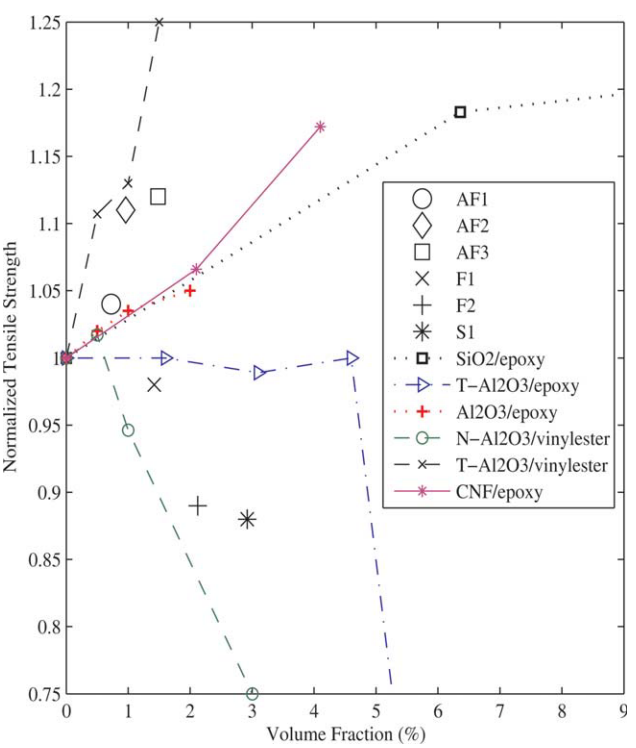

Figure 10 Comparison of these results for strength versus V_f to the reported trends for various fiber and particle nanocomposites. Sources: Ma[8] (dotted square), Zhao[11] (dashed dotted arrow), Naous[10] (dotted +), Guo[12] (dashed circle and dashed ×), and Iwahori[25] (solid asterisk). The T prefix represents treated particles. [Color figure can be viewed in the online issue, which is available at wileyonlinelibrary.com.]

versus V_f (reduced) graph (Fig. 9) showed the data for the nanofiber-based series collapsing to the alumina/epoxy modulus curve from Chen et al. This suggested that the fiber reinforcement had a comparable reinforcing efficiency but that the overall stiffening effect was reduced by the fiber fraction agglomerated into particles approaching the microscale. In contrast, the modulus associated with the narrower distribution of S1 alumina shifted little via the same method. More detailed property modeling, with a multiscale approach similar to that used for clay nanocomposites, could take advantage of a well-characterized distribution and illuminate the implications of this nanoheterogeneity.

Figure 10 provides a graph of strength versus V_f, showing distinctly different trends evident for the surface-modified and untreated particles. The results of Guo et al.[12] (dashed curves) were most consistent with those of this study and showed increasing strength with increasing V_f for surface-modified particles. This emphasized that strength was more sensitive than modulus to particle surface modification,[12,16] with surface modification permitting reinforcement by the mechanisms outlined previously.

However, unlike the consistent trends for modulus, significantly varied results have been published for the strengthening of polymers with nanoparticles. Also provided in Figure 10 are the results of three studies where strength was shown to moderately increase (spherical alumina/epoxy, dotted +; spherical silica, dotted square; and CNFs, solid asterisk) and one where a decrease was found despite surface modification (alumina/epoxy nanocomposite, dashed dotted arrow). Elucidation of the distribution of particles in these nanocomposites would permit a more complete understanding of these discrepancies.

CONCLUSIONS

Few polymer nanocomposites employ high-aspect-ratio nanofiber (nanowhisker) reinforcement. Fewer still use the nanofiber forms of metal oxides, such as alumina, despite their advantageous strength and stiffness characteristics. In this study, the use of nanofiber alumina particles was shown to improve both the tensile stiffness and strength of a two-part epoxy. Young's modulus increased by up to 19% at nanofiber V_f values of less than 1.5%, whereas strength increased up to 12% over the neat polymer.

The results corroborate the sensitivity of the strength to particle surface modification, as seen in other metal oxide particulate nanocomposites, and the relative insensitivity of the modulus to the same. Comparisons with published results revealed that the reinforcing efficiency of the nanofibers could be superior to that of monodispersed spherical silica and other nanocomposites reinforced with CNFs or spherical alumina particles.

An investigation of microstructure with a multiscale digital image analysis showed both well-dispersed primary particles and agglomerates of varied sizes. This characterization of the particle size distribution permitted enhanced interpretation of the material properties and was used for direct comparison to other nanocomposite systems.

The experiments reported here were carried out at the University of Alberta, where both authors were based at the time of the investigation. The authors acknowledge the insight and advice provided by Zihui Xia, Chingshen Li, and John Payzant. Technical aid was sought and gratefully obtained from Bernie Faulkner (Mechanical Engineering), Randy Mandryk (TEM, Biological Sciences) and George Braybrooke (SEM, Earth and Atmospheric Sciences) of the University of Alberta.

References

1. Ray, S. S.; Okamoto, M. Prog Polym Sci 2003, 28, 1539.
2. Luo, J. J.; Daniel, I. M. Compos Sci Tech 2003, 63, 1607.
3. Breuer, O.; Sundararaj, U. Polym Compos 2004, 25, 630.
4. Mahrholz, T.; Stängle, J.; Sinapius, M. Compos Appl Sci Manuf 2009, 40, 235.
5. Zhang, H.; Zhang, Z.; Friedrich, K.; Eger, C. Acta Mater 2006, 54, 1833.
6. Johnsen, B. B.; Kinloch, A. J.; Mohammed, R. D.; Taylor, A. C.; Sprenger, S. Polymer 2007, 48, 530.
7. Bondioli, F.; Cannillo, V.; Fabbri, E.; Messori, M. J Appl Polym Sci 2005, 97, 2382.
8. Ma, J.; Mo, M. S.; Du, X. S.; Rosso, P.; Friedrich, K.; Kuan, H. C. Polymer 2008, 49, 3510.
9. Cho, M.; Yang, S. Presented at 49th AIAA/ASME/ASCE/AHS/ASC Structures, Structural Dynamics and Materials Conference, Schaumburg, IL, 2008.
10. Naous, W.; Yu, X. Y.; Zhang, Q. X.; Naito, K.; Kagawa, Y. J Polym Sci B Polymer Phys 2006, 44, 1466.
11. Zhao, S.; Schadler, L. S.; Duncan, R.; Hillborg, H.; Auletta, T. Compos Sci Tech 2008, 68, 2965.
12. Guo, Z.; Pereira, T.; Choi, O.; Wang, Y.; Hahn, H. T. J Mater Chem 2006, 16, 2800.
13. Omrani, A.; Simon, L. C.; Rostami, A. A. Mater Chem Phys 2009, 114, 145.
14. Ozdilek, C.; Kazimierczak, K.; van der Beek, D.; Picken, S. J. Polymer 2004, 45, 5207.
15. Chen, C. H.; Jian, J. Y.; Yen, F. S. Compos Appl Sci Manuf 2009, 40, 463.
16. Vassileva, E.; Friedrich, K. J Appl Polym Sci 2006, 101, 4410.
17. Cao, M. S.; Zhou, W.; Shi, X. L.; Chen, Y. J. Appl Phys Lett 2007, 91, 021912.
18. Medina, R.; Haupert, F.; Schlarb, A. K. J Mater Sci 2008, 43, 3245.
19. Chatterjee, A.; Islam, M. S. Mater Sci Eng 2008, 487, 574.
20. Ng, C. B.; Schadler, L. S.; Siegel, R. W. Nanostruct Mater 1999, 12, 507.
21. Thostenson, E. T.; Li, C. Y.; Chou, T. W. Compos Sci Tech 2005, 65, 491.
22. Njuguna, J.; Pielichowski, K.; Alcock, J. R. Adv Eng Mater 2007, 9, 835.
23. Mahfuz, H.; Adnan, A.; Rangari, V. K.; Jang, B.; Jeelani, S. Compos Appl Sci Manuf 2004, 35, 519.
24. Xu, J.; Donohoe, J. P.; Pittman, C. U. Compos Appl Sci Manuf 2004, 35, 693.
25. Iwahori, Y.; Ishiwata, S.; Sumizawa, T., Ishikawa, T. Compos Appl Sci Manuf 2005, 36, 1430.

26. Prolongo, S. G.; Burón, M.; Gude, M. R.; Chaos-Morán, R.; Campo, M.; Ureña, A. Compos Sci Tech 2008, 68, 2722.
27. Sandler, J.; Werner, P.; Shaffer, M. S. P.; Demchuk, V.; Altstädt, V.; Windle, A. Compos Appl Sci Manuf 2002, 33, 1033.
28. Brechet, Y.; Cavaille, J. Y.; Chabert, E.; Chazeau, L.; Denievel, R.; Flandin, L.; Gauthier, C. Adv Eng Mater 2001, 3, 571.
29. Capadona, J. R.; Shanmuganathan, K.; Trittschuh, S.; Seidel, S.; Rowan, S. J.; Weder, C. Biomacromolecules 2009, 10, 712.
30. Miyagawa, H.; Mohanty, A.; Lawrence, T. D.; Misra, M. Ind Eng Chem Res 2004, 43, 7001.
31. Brown, G. M.; Ellyin, F. J Appl Polym Sci 2005, 98, 869.
32. Yang, F.; Bogdanova, I.; Wang, K. G.; Nelson, G. L. Presented at SAMPE '07: M and P – From Coast to Coast and Around the World, Baltimore, MD, 2007.
33. Liu, S.; Zhang, H.; Zhang, Z.; Zhang, T.; Sprenger, S. Polym Polym Compos 2008, 16, 527.
34. Wong, M.; Paramsothy, M.; Xu, X. J.; Ren, Y.; Li, S.; Liao, K. Polymer 2003, 44, 7757.
35. Morgan, A. B.; Gilman, J. W. J Appl Polym Sci 2002, 87, 1329.
36. Wang, L.; Wang, K.; Chen, L.; Zhang, Y. W.; He, C. B. Compos Appl Sci Manuf 2006, 37, 1890.
37. Bhimaraj, P.; Burris, D. L.; Action, J.; Sawyer, W. G.; Toney, C. G.; Siegel, R. W.; Schadler, L. S. Wear 2005, 258, 1437.
38. Wosik, J.; Dubiel, B.; Kruk, A.; Penkalla, H.; Schubert, F.; Czyrska-Filemonowicz, A. Mater Char 2001, 46, 119.
39. Sigalov, G.; Ibuki, J.; Chiba, T.; Inoue, T. Macromolecules 1997, 30, 7759.
40. Jenni, A.; Herwegh, M.; Zurbriggen, R.; Aberle, T.; Holzer, L. J Microsc 2003, 212, 186.
41. Ratinac, K. R.; Zhu, H. Y.; Stadtmueller, L. M.; Ringer, S. P. Mater Forum 2002, 26, 44.
42. Aktas, L.; Hamidi, Y. K.; Altan, M. C. J Eng Mater Tech 2008, 130, 031005–01.
43. Sheng, N.; Boyce, M.; Parks, D.; Rutledge, G.; Abes, J.; Cohen, R. Polymer 2004, 45, 487.
44. Loo, L. S.; Gleason, K. K. Polymer 2004, 45, 5933.
45. Ratinac, K. R.; Gilbert, R. G.; Ye, L.; Jones, A. S.; Ringer, S. P. Polymer 2006, 47, 6337.
46. Vermogen, A.; Masenelli-Varlot, K.; Séguéla, R.; Duchet-Rumeau, J.; Boucard, S.; Prele, P. Macromolecules 2005, 38, 9661.
47. Dominkovics, Z.; Renner, K.; Pukánszky, B. Macromol Symp 2008, 267, 52.
48. Li, C. S.; Ellyin, F.; Koh, S.; Oh, S. J. Mater Sci Eng A 2000, 276, 218.
49. Brandon, D.; Kaplan, W. Microstructural Characterization of Materials; Wiley: Toronto, Canada, 1999.
50. Ramachandran, V.; Beaudoin, J. In Image Analysis; Darwin, D., Ed.; Noyes: Westwood, NJ, 2001; Chapter 19.